

Mode-Dependent Phonon Relaxation in fcc Ni: Insights from Molecular Dynamics Simulations with Frozen-Trajectory Excitations

Wojciech Marciniak*

*Institute of Physics, Poznan University of Technology, Piotrowo 3, 60-965 Poznań, Poland
Department of Physics and Astronomy, Uppsala University, P.O. Box 516, 75120 Uppsala, Sweden and
Institute of Molecular Physics, Polish Academy of Sciences,
M. Smoluchowskiego 17, 60-179 Poznań, Poland*

Joanna Marciniak

*Institute of Molecular Physics, Polish Academy of Sciences,
M. Smoluchowskiego 17, 60-179 Poznań, Poland and
Department of Physics and Astronomy, Uppsala University, P.O. Box 516, 75120 Uppsala, Sweden*

José Ángel Castellanos-Reyes and Jan Ruzs

*Department of Physics and Astronomy, Uppsala University, P.O. Box 516, 75120 Uppsala, Sweden
(Dated: October 1, 2024)*

We present a computational study of phonon relaxation in face-centered cubic (fcc) nickel (Ni), focusing on ultra-fast magnetization dynamics. The phonons are excited beyond their thermal equilibrium population, and the relaxation behavior is analyzed as a function of both wave vector (\vec{q}) and phonon frequency (ω). To efficiently investigate these excitations, we introduce a trajectory post-processing technique, the *frozen-trajectory excitation*, which facilitates the (\vec{q}, ω) -resolved analysis. Molecular dynamics simulations combined with the frozen-phonon multislice method predict relaxation signatures observable with time-resolved transmission electron microscopy (TEM) at 10–20 fs resolution. Our findings indicate mode dependence in the relaxation processes, highlighting the importance of phonon-specific behavior consideration in ultrafast dynamics.

I. INTRODUCTION

In 1996, Beaurepaire *et al.* first reported an ultra-fast demagnetization process in face-centered cubic (fcc) nickel [1], where a femtosecond laser pulse caused a rapid decrease in magnetization within a few hundred femtoseconds, followed by a much slower return to equilibrium. This discovery generated considerable interest, driven by the potential for magnetization switching on sub-picosecond timescales, which holds promise for future technological applications. To explain these observations, the three-temperature model was introduced in Ref. [1], describing the dynamics of three coupled reservoirs – spins, crystal lattice, and electrons – each exhibiting distinct effective temperatures. Various extensions of this model have been proposed [2–4]. However, despite almost three decades of research, the role of lattice dynamics in the ultra-fast demagnetization process has received comparatively little attention, with much of the focus being placed on the spin and electron systems [5, 6]. Recent experimental and theoretical works have increasingly demonstrated the importance of lattice dynamics in this process [7–10].

Advances in transmission electron microscopy (TEM) technology over recent decades – including aberration corrections [11, 12], efficient electron beam monochromatization allowing to resolve vibrational modes [13], direct electron detectors [14, 15], as well as the recent incorporation of laser pulses with decreasing time scales and

fast cameras [16–19] – have opened the door to ultra-fast studies at spatial resolutions down to the atomic scale. These technological developments suggest that ultra-fast studies of phonon dynamics using electron energy loss spectroscopy (EELS) may soon become possible.

In this work, we present a computational study on the ultra-fast dynamics of phonons in fcc Ni, focusing on phonon relaxation after excitation beyond thermal equilibrium. We employ molecular dynamics (MD) simulations using the LAMMPS package [20] and introduce a novel method we refer to as *frozen-trajectory excitation* (for details, see Sec. II), which allows us to resolve phonon excitations as a function of both wave vector (\vec{q}) and phonon frequency (ω) by manipulation on the saved, ‘frozen’ MD trajectory. This method is efficient and flexible, capable of being applied to both atomic (MD) and magnetic dynamics – e.g., atomistic spin dynamics (when applied to magnetic moments and magnetic torques). After excitation, we simulate the free relaxation of the system over several picoseconds, analyzing the evolution of diffraction patterns using the frozen-phonon multislice method [21] as implemented in DR-PROBE [22]. The results reveal clear signatures of multi-phonon scattering processes and show that phonon relaxation is highly mode-dependent, corroborating the mode-dependent phonon-phonon interaction life-times calculated in Ref. [9]. This highlights that quantities averaged over the full Brillouin zone, like the phonon relaxation times, can mask the underlying rich mode-specific dynamics.

The theoretical framework developed in this work is a natural extension of the frequency-resolved frozen

* email: wojciech.marciniak@put.poznan.pl

phonon multislice (FRFPMS) method [23, 24] in a way that allows for arbitrary excitations and subsequent reconstructions of complete molecular dynamics trajectories for further free relaxation simulations.

II. CALCULATION DETAILS

II.1. Overview

Our calculations consist of three main phases, as shown in Fig. 1, which were performed using an in-house software designed to integrate LAMMPS via its “as a library” feature [20]. In the first phase, the system is created and equilibrated using LAMMPS subroutines. Next, in the second phase, we obtain the time-dependent position $\vec{r}(t)$ (trajectory) during the equilibrium finite-temperature simulations of the system from LAMMPS. This trajectory is then manipulated using the FFTW3 fast Fourier transform (FFT) library [25], following the procedure detailed below, to introduce the desired excitation. In the final phase, we allow for a free molecular dynamics relaxation of the excited vibrations, after which the resulting trajectories are analyzed using the DRPROBE scanning transmission electron microscopy (STEM) image simulations software [22] to simulate time-resolved electron diffraction patterns.

To ensure computational efficiency and cost-effectiveness, we described the interatomic interactions with the spectral neighbor analysis pattern machine-learning interatomic potential (SNAP ML-IAP [26], referred to further as SNAP) in the parametrization of Zuo *et al.* [27].

II.2. System creation and equilibration

All initial simulations were conducted using the LAMMPS `fix-es` with integration schemes based on the time-reversible measurement-preserving Verlet and rRESPA integrators by Tuckerman *et al.* [28]. In the unconstrained MD simulations, we employed the pure velocity-Verlet integrator. A consistent time step of 1 fs was used throughout all simulations.

We considered a $28 \times 28 \times 28$ supercell of conventional 4-atom fcc Ni cells oriented along the (001) crystal direction. The lattice parameter was optimized using the isothermal-isobaric (NpT) ensemble, resulting in $a = 3.5329$ Å at 300 K. With this optimized a , the calculations were restarted in the canonical (NVT) ensemble, and atomic velocities were randomized using the Maxwell-Boltzmann distribution at 600 K (overestimated to expedite equilibration). The system was then equilibrated for 2 ps at the target temperature of 300 K. Both the NpT and NVT stages employed the Nosé-Hoover thermostat and barostat [29], with the equations of motion based on the implementation by Shinoda *et al.* [30].

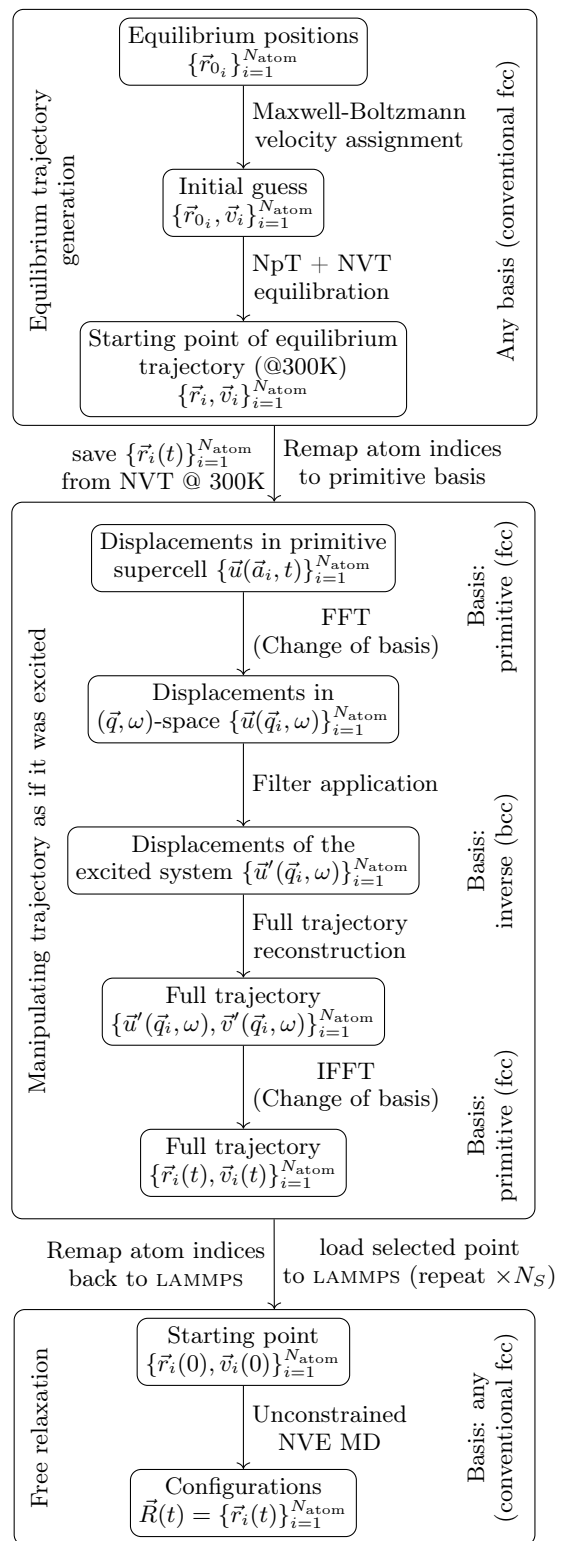


FIG. 1: Schematic overview of the calculations workflow presenting steps performed to obtain atomic configurations at different time delays during the relaxation process. It shows explicitly performed changes of basis from cartesian space (\vec{r}, t) , via the primitive cells (\vec{a}, t) and (\vec{q}, ω) , and back.

II.3. Equilibrium trajectory

After initial equilibration, we performed simulations spanning 1 ps within the canonical (NVT) ensemble, saving atomic configurations – referred to as *snapshots* – at regular time intervals. We refer later to this stage as equilibrium trajectory gathering. Each atom’s trajectory from LAMMPS was decomposed into three components: the origin of the unit cell \vec{r}^0 , the atomic displacement \vec{u} , and the basis site position \vec{b} . Explicitly,

$$\vec{r}_{h,k,l,i}(t) = \vec{r}_{h,k,l}^0 + \vec{b}_i + \vec{u}_{h,k,l,i}(t), \quad (1)$$

where i is the unit cell basis index, and h , k , and l are indices for the unit cells within the supercell, corresponding to integer multiples of the lattice vectors \vec{a}_1 , \vec{a}_2 , and \vec{a}_3 . The atomic positions \vec{r} and displacements \vec{u} are functions of the unit cell indices h , k , and l , as well as time (t). The basis site positions \vec{b}_i are independent of time and the unit cell indices within the supercell. Therefore, the displacements \vec{u} can be represented in an 8-dimensional hypercube. At later stages, the Cartesian coordinates x , y , and z are treated equivalently. We remap the atomic indices into a supercell of primitive unit cells ($i = 0$), simplifying this to a 4-dimensional hypercube for subsequent transformations. We employ the index order $\mathbf{u}[\{\mathbf{x}=0, \mathbf{y}=1, \mathbf{z}=2\}][\mathbf{i}][\mathbf{h}][\mathbf{k}][\mathbf{l}][\mathbf{n}]$ (where n is the snapshot index for time t) to facilitate efficient reuse of the data array during the 4D (\vec{r}, t) \rightarrow (\vec{q}, ω) and 1D (t) \rightarrow (ω) Fourier transforms, without requiring additional memory padding.

Prior to performing Fourier transforms, we apply a Tukey window (cosine-tapered window) $W[n]$ to reduce the effects of trajectory discontinuities in time [31]:

$$W[n] = \begin{cases} \frac{1}{2} [1 - \cos(\frac{2\pi n}{\alpha N})], & \text{if } 0 \leq n \leq \frac{\alpha N}{2} \\ 1, & \text{if } \frac{\alpha N}{2} \leq n \leq \frac{N}{2} \\ W[N - n], & \text{otherwise.} \end{cases} \quad (2)$$

Here, cosine decay is applied to the α portion of the trajectory both in the beginning and at the end of the equilibrium MD simulation, resulting in the removal of the first and last 99 snapshots from the total of 500 snapshots.

At this point, we transform the superlattice into one of primitive fcc unit cells, given by the vectors:

$$\begin{aligned} \vec{a}_1 &= (0.5a, 0.5a, 0) \\ \vec{a}_2 &= (0.5a, 0, 0.5a) \\ \vec{a}_3 &= (0, 0.5a, 0.5a), \end{aligned}$$

resulting in a supercell of $56 \times 56 \times 28$ primitive unit cells.

With the saved trajectories, we can evaluate the accuracy of the simulations by calculating the phonon dispersion and comparing it with experimental results. Typically, phonon dispersions are obtained from MD trajectories via a Fourier transform \mathcal{F} of the velocity autocorrelation function [33]. However, in this study, we approximate phonon dispersion using atomic displacements

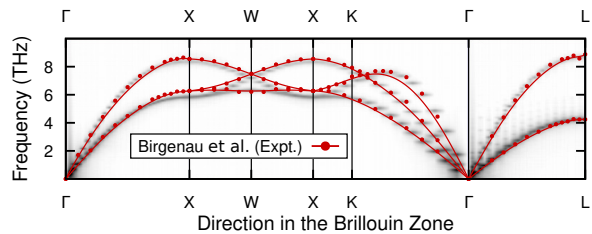


FIG. 2: Comparison of the phonon dispersion in fcc Ni with experimental data from Birgenau *et al.* [32]. The phonon dispersion has been calculated from atomic displacements according to Eq. 3, with normalized intensities.

only:

$$I(\vec{q}, \omega) = |\mathcal{F}(\vec{u}(\vec{r}^0, t))|, \quad (3)$$

which is computationally equivalent to using velocity autocorrelation, up to a constant [34] [35]. In discrete form, the phonon dispersion can be written as:

$$I[q_x, q_y, q_z, \omega] = |FFT(\vec{u}[h, k, l, n])|, \quad (4)$$

where n is the MD frame number. We compare it to the experimental results by Birgenau *et al.* [32] and show the comparison in Fig. 2. The phonon dispersion calculated from our simulations shows excellent agreement with the experimental results. We achieve accuracy comparable to density functional theory (DFT) calculations while significantly reducing computational costs. By utilizing GPU acceleration and generating multiple trajectories from a single equilibrium trajectory, we realize an efficiency improvement of three to four orders of magnitude over traditional CPU-only calculations, which rely on a one-excitation-per-trajectory approach. It is noteworthy that, similar to the FRFPMS method, our approach relies on molecular dynamics (MD) simulations, which scale linearly, i.e., $\mathcal{O}(n)$, with the number of atoms in the system.

II.4. Excitation

After calculating $\vec{u}(\vec{q}, \omega)$, we introduce an excitation into the system by manipulating these displacements. Specifically, we adjust $\vec{u}(\vec{q}, \omega)$ to create a modified displacement field $\vec{u}'(\vec{q}, \omega)$, corresponding to an excited state. This is achieved by applying a band-pass filter $F(\vec{q}, \omega)$ to $\vec{u}(\vec{q}, \omega)$, amplifying the displacement by a factor of $(A - 1)$, and then adding it to the original signal, resulting in an overall enhancement by a factor of A in the desired (\vec{q}, ω) region:

$$\vec{u}'(\vec{q}, \omega) = \vec{u}(\vec{q}, \omega) + (A - 1) [F(\vec{q}, \omega)\vec{u}(\vec{q}, \omega)]. \quad (5)$$

This general transformation allows us to simulate an out-of-equilibrium state, where a specific range of phonon modes is overpopulated thermally.

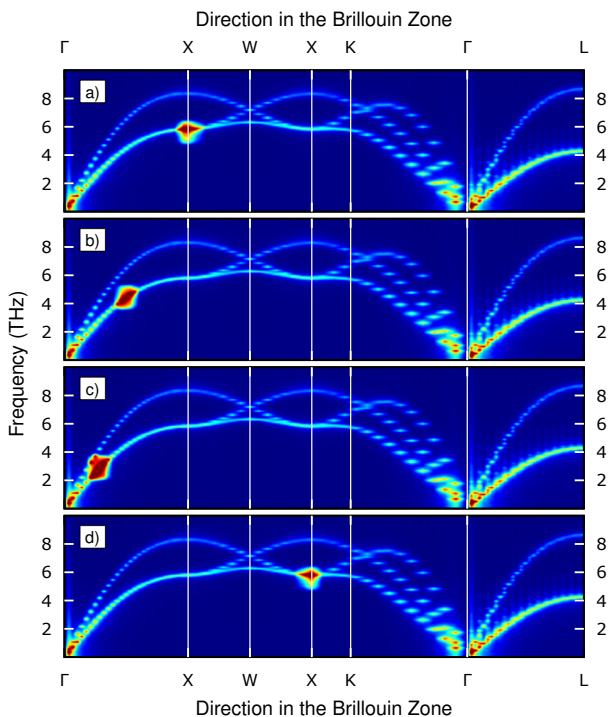


FIG. 3: Phonon dispersion of fcc Ni after applying the simulated excitation filter. Panels (a) and (c) show excitations at X high-symmetry points in the Brillouin zone along the \hat{q}_y and \hat{q}_z directions. Panels (b) and (d) depict arbitrary excitations along the Δ high-symmetry line in the \hat{q}_y direction. Intensities are normalized.

The band-pass filter F is multiplicative and based on the cosine-tapered window function (Tukey window):

$$F[h][k][l][n] = F[h] \cdot F[k] \cdot F[l] \cdot F[n], \quad (6)$$

where for every index i varying between 0 and M_i , the partial functions:

$$F[i] = \begin{cases} 0, & \text{if } |i_0 - i| > (\Delta_i + \alpha_i)M_i \\ 1, & \text{if } |i_0 - i| < \Delta_i M_i \\ \frac{1}{2} \left[1 - \cos \left(\frac{\pi(\alpha_i M_i - |i_0 - i| + \Delta_i M_i)}{\alpha_i M_i} \right) \right], & \text{otherwise} \end{cases} \quad (7)$$

specify a window centered at i_0 , with a width of $\Delta_i M_i$, and decaying over a fraction α_i of the M_i range. The filter is then multiplied by its hermitian conjugate in \vec{q} and ω in a way that ensures its hermiticity.

We excite longitudinal acoustic (LA) phonons at four distinct points in the $q_z = 0$ plane of the reciprocal space. These points include the high-symmetry X point in both the \hat{q}_y and \hat{q}_z directions, as well as two intermediate points along the Δ high-symmetry line. The phonon dispersion after applying the filter is shown in Fig. 5(a-d).

Up to this point, memory usage is minimized by storing only the atomic positions. This allows all calculations to be performed in an efficient and scalable way using only RAM. However, to continue molecular dynamics simulations after introducing the excitation, we require a full set

of coordinates $\vec{R}_N = \{\{\vec{r}_i, \vec{v}_i\}\}_{i=1}^{N_{\text{atom}}}$, where both atomic positions and velocities are included. To reconstruct the velocities, we treat velocity as the time derivative of position (and thus displacement):

$$\begin{aligned} \vec{v}(\vec{r}, t) &= \frac{d\vec{u}(\vec{r}, t)}{dt} \\ \vec{v}(\vec{q}, \omega) &= -i\omega\vec{u}(\vec{q}, \omega), \end{aligned} \quad (8)$$

which corresponds to rescaling by a factor of ω and introducing a 90-degree phase shift, resulting in a highly efficient *swap-and-multiply* transformation:

$$\begin{aligned} \text{Re}[\vec{v}(\vec{q}, \omega)] &= \omega \text{Im}[\vec{u}(\vec{q}, \omega)] \\ \text{Im}[\vec{v}(\vec{q}, \omega)] &= -\omega \text{Re}[\vec{u}(\vec{q}, \omega)]. \end{aligned} \quad (9)$$

From here, we recover $\vec{v}(t)$ and $\vec{u}(t)$ through inverse Fourier transforms, and converting displacements back into atomic positions is straightforward.

From a modified trajectory, we select N_s snapshots for further unconstrained NVE relaxation. In this work, we chose snapshots spaced 100 fs apart (i.e., $N_s = 7$), so that they are no longer correlated due to the influence of the thermostat. Depending on the specific simulation scheme, we repeated the procedure 7 or 14 times, resulting in $N = 49$ or 98 uncorrelated relaxation events, respectively. In the initial stage of the study, 100 snapshots were saved at 10 fs intervals. In the later stages, the sampling count was increased to 200 frames, with the time interval extended to 20 fs.

With a sampling period of 10 fs for equilibrium trajectory gathering, this procedure resulted in less than 0.2% relative error in the reconstructed velocities (assuming $v \not\approx 0$), while nearly halving memory usage. This error – estimated by comparing velocities calculated by LAMMPS with those reconstructed from Eqs. 9 for a trajectory without excitation – did not significantly increase when the sampling period was extended to 20 fs. Hence, in this work, we use 20 fs sampling period and 500 frames during the equilibrium trajectory gathering.

II.5. Diffraction patterns calculation

The snapshots obtained from the free molecular dynamics simulations are used to calculate electron diffraction patterns within the frozen-phonon multislice (FPMS) framework [21], using a parallel incident electron beam at acceleration voltage of 100 kV. The exit electron wavefunction – which in general can depend on the in-plane momentum transfer \vec{q}_\perp , the electron beam position \vec{r}_b , and the atomic configuration $\vec{R} = \{\vec{r}_i\}_{i=1}^{N_{\text{atom}}}$ – is computed for each of the 49 (or 98) independent NVE relaxations and for each time frame during the recorded relaxation using DRPROBE.

For each relaxation time frame, we calculate the thermal diffuse scattering (inelastic phonon scattering) contribution to the diffraction patterns using the quantum

excitation of phonons (QEP) framework [36, 37]:

$$I_{\text{incoh}}(\vec{q}_{\perp}, \vec{r}_b, t) = \frac{1}{N} \sum_{j=1}^N |\psi(\vec{q}_{\perp}, \vec{r}_b, \vec{R}_j(t))|^2 \quad (10)$$

$$I_{\text{coh}}(\vec{q}_{\perp}, \vec{r}_b, t) = \left| \frac{1}{N} \sum_{j=1}^N \psi(\vec{q}_{\perp}, \vec{r}_b, \vec{R}_j(t)) \right|^2 \quad (11)$$

$$I_{\text{vib}}(\vec{q}_{\perp}, \vec{r}_b, t) = I_{\text{incoh}}(\vec{q}_{\perp}, \vec{r}_b, t) - I_{\text{coh}}(\vec{q}_{\perp}, \vec{r}_b, t), \quad (12)$$

where I_{incoh} , I_{coh} , and I_{vib} represent the incoherent (total) scattering intensity, the coherent (elastic) intensity, and the vibrational intensity, respectively. For a detailed description of how to calculate ω -resolved I_{vib} and angle-resolved electron energy loss spectra using the FRFPMS method, we refer the reader to Ref. [24]. In our case, since we consider a plane-wave illumination, the results are independent of \vec{r}_b . Nevertheless, the scheme is also directly applicable in the context of STEM.

Figure 4 shows the calculated electron diffraction pattern contributions, including the coherent (a), incoherent (b), and vibrational (c) components, based on 350 snapshots sampled from an NVT trajectory before excitation and NVE relaxation. In Fig. 4(a), minor noise is visible around the Bragg spots. This noise results from incomplete sampling of the system's configurational space and should approach zero with infinite statistics. Importantly, the noise is approximately two orders of magnitude weaker than the vibrational intensity in these regions, as shown in Fig. 4(c). Additionally, forbidden reflections can be observed. These occur because the distribution of atoms in individual atomic planes differs from that of atoms in a z -projected unit cell. Beam propagation effects cause imperfect destructive interference, leading to the appearance of these kinematically forbidden Bragg spots, albeit at low intensity.

III. RESULTS AND DISCUSSION

So far, we have not explicitly discussed the rationale behind the selection of the excitation points. The high-symmetry point X was chosen because it is the only high-symmetry point where reflections of all its equivalent copies ($X_{\hat{q}_x}$, $X_{\hat{q}_y}$, and $X_{\hat{q}_z}$) can be observed in the detection plane, see Fig. 4(c). Additionally, excitation points along the Δ high-symmetry line in the \hat{q}_y direction – specifically, halfway between the Γ and X high-symmetry points, and at half the frequency of the X point – enable us to observe momentum and energy transfers during the relaxation process.

Figure 5 presents the diffraction patterns at the very beginning of the relaxation process. The excitations appear as intensity peaks at their corresponding \vec{q}_{\perp} values. In panels 5(b) and 5(c), additional reflections are observed at double the \vec{q} of the induced excitation (highlighted by red ellipses). In the initial frame (0^{th} frame), we can confidently conclude that this effect is not caused by a higher-than-thermal excitation of phonon modes

with double momentum transfer, as the phonon dispersion and population statistics are well-resolved. Therefore, these additional local intensity maxima can only be attributed to multi-phonon scattering processes.

The excitation peaks in the diffractograms are all elongated in the $(1, -1)$ direction. This results from the cubic filter ($\Delta q_{a_1} = \Delta q_{a_2} = \Delta q_{a_3}$) applied in the primitive coordinate system:

$$\begin{aligned} \vec{q}_{a_1} &= (a^{-1}, -a^{-1}, a^{-1}), \\ \vec{q}_{a_2} &= (a^{-1}, a^{-1}, -a^{-1}), \\ \vec{q}_{a_3} &= (-a^{-1}, a^{-1}, a^{-1}). \end{aligned}$$

When described in Cartesian coordinates, this cubic filter transforms into a rhombohedron with its short diagonal aligned along the (111) direction in reciprocal space. The projection of this rhombohedron onto the (001) plane in the \vec{q} -space specified in the cartesian basis is what is observed in all panels of Fig. 5.

Therefore, for further analysis, we integrate the vibrational intensities over an aperture Ω :

$$I_{\text{vib}}[\Omega(\vec{q}_{\perp}), \vec{r}_b] = \iint_{\Omega(\vec{q}_{\perp})} I_{\text{vib}}(\vec{q}_{\perp}, \vec{r}_b) d\vec{q}_{\perp}, \quad (13)$$

where the aperture Ω is an elliptical region and is defined by:

$$\begin{aligned} \Omega(\vec{q}_{\perp}) : & \frac{[(q_x - q_{x0}) \cos \alpha + (q_y - q_{y0}) \sin \alpha]^2}{a^2} + \\ & + \frac{[(q_x - q_{x0}) \sin \alpha + (q_y - q_{y0}) \cos \alpha]^2}{b^2} \leq 1, \end{aligned} \quad (14)$$

where α is the tilt angle (45°), and the semiaxes are $a = 4$ px and $b = 3$ px ($\sim 0.08 \times 0.06 \text{ \AA}^{-1}$). The origin point is (q_{x0}, q_{y0}) . The ellipses are shown in Fig. 5, with colors corresponding to the intensity-versus-time plots in Figs. 6 and 7.

Fig. 6 presents the first 1 ps of the relaxation process of two of the selected excitations with a temporal resolution of 10 fs. The diffractograms are averaged over 98 uncorrelated relaxation trajectories realized according to the procedure described in Sec. II.4. There are two key observations. Firstly, the excitation in between the Γ and $X_{\hat{q}_y}$ points (Fig. 6(b)) relaxes significantly faster than the excitation in $X_{\hat{q}_y}$ point (Fig. 6(a)). In Fig. 6(b), the yellow curve drops by approximately 60% of its initial value within the first picosecond, while the corresponding excitation in Fig. 6(a) decreases by less than 15% over the same period. Interestingly, this faster relaxation is accompanied by an intensity enhancement at double the excitation point's \vec{q} (see the red curve in Fig. 6(b)). This may indicate ongoing energy transfer to phonon modes associated with the X-point. This behavior differs from the multi-phonon excitations seen in Fig. 5, as scattering from the excited modes decreases over time, and the two-phonon scattering should also diminish. However, a mild but distinct intensity increase is observed up to around 600–700 ps. Secondly, we observe oscillations in

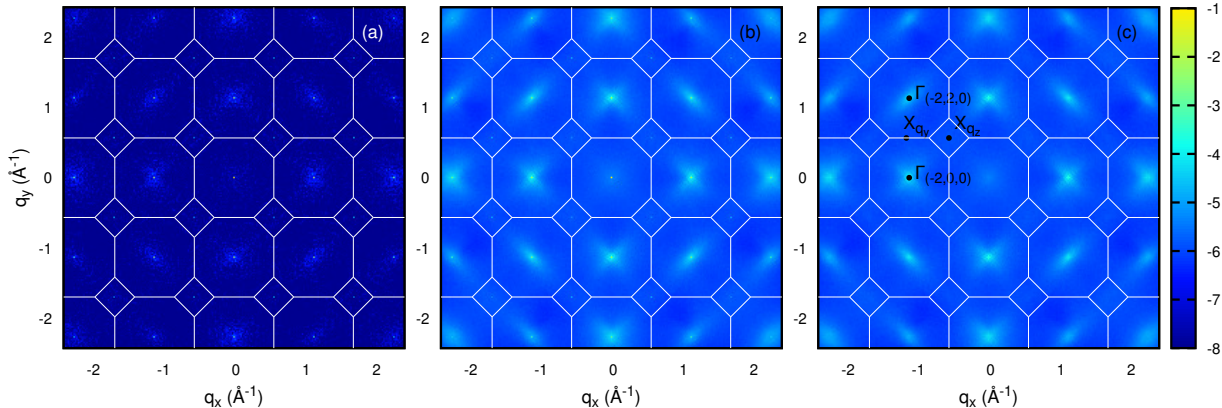


FIG. 4: Coherent (a) and incoherent (b) averages of exit wavefunctions over 196 atomic configurations in simulated electron spectroscopy, using a parallel beam incident on an fcc Ni supercell ($28 \times 28 \times 28$ conventional 4-atom unit cells) in thermodynamic equilibrium at 325 K. Panel (c) shows the thermal diffuse (inelastic) scattering diffraction pattern.

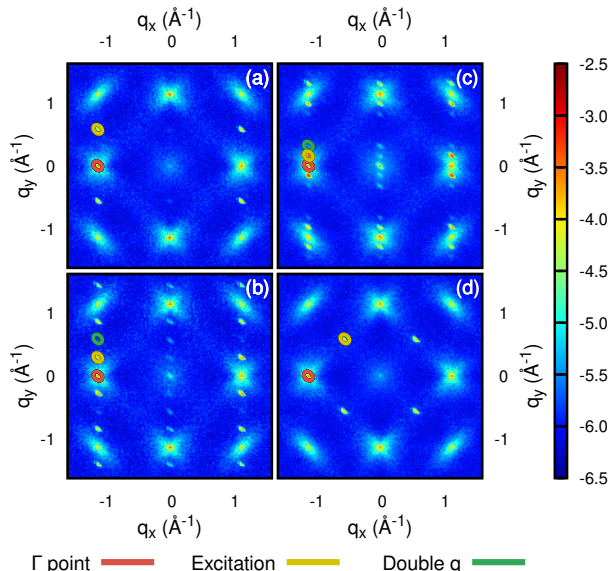


FIG. 5: Diffraction patterns of the excited system before relaxation: (a) Excitation at the X-point in the \hat{q}_y direction. (b) Excitation along the Δ high-symmetry line in the \hat{q}_y direction, halfway between the Γ and X high-symmetry points. (c) Excitation along the Δ high-symmetry line in the \hat{q}_y direction, at half the frequency of the X-point; (d) Excitation at the X-point in the \hat{q}_z direction, see Fig. 4(a). The colored ellipses indicate the integration areas for intensity plots, which are presented in subsequent figures with corresponding colored lines.

the vibrational intensity in the excitation point, occurring at double the frequency of the excited phonon mode.

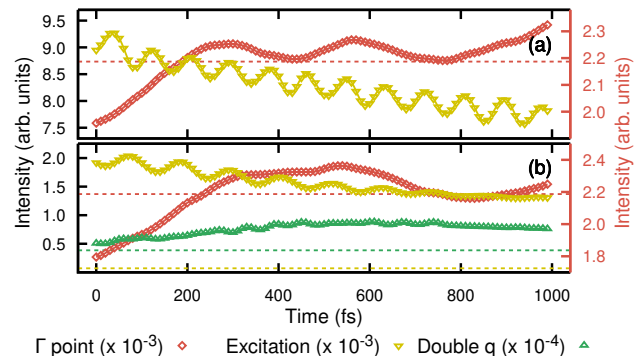


FIG. 6: Integrated diffraction intensities over a 1 ps trajectory with a sampling period of 10 fs. Panel (a) shows the relaxation of the excitation at the X-point in the \hat{q}_y direction. Panel (b) depicts the relaxation of the excitation along the Δ high-symmetry line in the \hat{q}_y direction, halfway between the Γ and X points, and reveals an energy transfer to the X-point. The plots represent the relaxation processes of the excitations shown in Fig. 5, with colors and panel order corresponding to that figure. Dashed lines denote the equilibrium values at 325 K. In panel (a), the equilibrium value for the intensity integrated over the excitation point (yellow curve) is located at the value of 3.85×10^{-5} , which is well outside the plot range.

Those are related to structured noise stemming from the incompleteness of configuration space sampling. On the other hand, it is noteworthy that similar intensity oscillations have been previously reported at the Γ -point in bismuth [38–42].

Two factors currently limit the experimental observation of the behavior we describe in this work. First, there is no existing method for \vec{q} -resolved phonon excitation

in scanning transmission electron microscopy. Second, current hardware capabilities are only now approaching the temporal resolution necessary to observe these effects [38]. Since observed intensities come from squared electron-beam exit wave-functions, the frequency of oscillations is twice the frequency of phonon modes observable at given scattering angles.

The X-point intensity enhancement presents a more complex scenario, as it may reflect energy transfer, resonant multi-phonon excitation at a specific frequency, or both. If this effect is indeed associated with energy transfer via the X-point – and we provided an argument in favor of this explanation – it suggests that the relaxation time constant τ is not only strongly dependent on (\vec{q}, ω) , but is also governed by intricate phonon-phonon interactions. This indicates that, in addition to phonon and phonon-magnon interactions, phonon-phonon interactions must also be considered when analyzing the system’s magnetization dynamics. Regardless, the strong (\vec{q}, ω) -dependence of τ is undeniable.

Since the excitations after the 1 ps are clearly not equilibrated, we decided to repeat the simulations for a longer but less detailed trajectory spanning 4 ps, with a sampling period of 20 fs. We also expanded the range of excited points in (\vec{q}, ω) space by introducing excitations at the X high-symmetry point in the \hat{q}_z direction – observable as reflections in the (1,1) direction of the diffraction pattern – and along the Δ high-symmetry line in the \hat{q}_y direction, where phonon modes have frequencies equal to half of the acoustic phonons at the X point. These repeated calculations also served to cross-check the results shown in Fig. 6. The results, presented in Fig. 7, are averaged over 49 new uncorrelated trajectories with different random seeds, with excitations introduced as described in Sec. II.4. Fig. 8 shows a 3D view of this evolution of the Δ scan intensity in time and depicts the true magnitude of oscillations relative to the excitation amplitude. Over this extended period, the difference in relaxation timescales between X-point excitations (Fig. 7(a,d), Fig. 8 (a)) and arbitrary excitations along the Δ high-symmetry line (Fig. 7(b,c), Fig. 8 (b,c)) becomes even more pronounced.

Additionally, Figs. 7(b) and 7(c) reveal a beat in the vibrational intensity oscillations at the excitation point. This beat arises due to the finite size of both the excitation filter and the aperture used for integrating the intensity. The effect is more pronounced in Fig. 7(c) because the excitation captures the transverse acoustic mode at the same \vec{q} , resulting in the effective summation of vibrational intensities from two distinct phonon modes. Nevertheless, Fig. 7(b) also shows that the enhancement affects a range of phonon wave vectors and frequencies, which are integrated over the aperture. Consequently, this beat should disappear for a point excitation (or point aperture). As the vibrations stem from a structured noise, this behavior should also become negligible with sufficient sample averaging.

After 4 ps, the excitations are mostly relaxed – especially those shown in Fig. 7(b) (also Fig. 8(b)), halfway

between the Γ and $X_{\hat{q}_y}$ high-symmetry points. The relaxation of the X longitudinal acoustic (LA) mode at half its frequency likely reaches its half-life due to interactions between multiple excited phonons. In contrast, the intensity of excitations at $X_{\hat{q}_y}$ and $X_{\hat{q}_z}$ decreases by only around 25 – 30% over the same period. The resulting relaxation plots are challenging to fit with a decaying exponential function, likely due to intricate phonon-phonon interactions.

The τ derived from the three-temperature model is an effective average over the Brillouin zone. However, our results demonstrate that the contributions to this average are strongly (\vec{q}, ω) -dependent. In particular, the relaxation observed in Fig. 7(b) (also Fig. 8(b)) mostly occurs within the first picosecond, whereas the phonons excited at the X high-symmetry point exhibit a much longer relaxation period. This observation aligns with the time scales reported by Pankratova *et al.* [4] as well as with the mode-dependent relaxation times due to phonon-phonon interactions reported by Ritmann *et al.* [9].

IV. SUMMARY AND CONCLUSIONS

In this work, we presented a novel approach for exploring phonon relaxation processes through molecular dynamics simulations combined with frozen-phonon multislice calculations. This method enables a (\vec{q}, ω) -resolved analysis of phonon dynamics, emphasizing the mode-dependence of relaxation times. By introducing the frozen-trajectory excitation technique, we achieved efficient and flexible manipulation of atomic trajectories, allowing selective excitation of specific phonon modes in face-centered cubic nickel.

Our findings demonstrate that the relaxation process is highly dependent on the phonon mode. In particular, excitations at the X-point exhibit slower relaxation compared to intermediate excitations along the Δ high-symmetry line. This mode-specific dependence indicates that traditional approaches to phonon relaxation, which often average over the entire Brillouin zone, may obscure important mode-resolved behaviors in real materials. We confirm expected structured noise patterns and effects observable in simulated time-resolved transmission electron microscopy – related to sample count, excitation region, and integration aperture. These results offer new avenues for investigating ultrafast phonon dynamics in real materials and contribute to a deeper understanding of the role of phonons in ultrafast magnetization dynamics and energy dissipation mechanisms.

ACKNOWLEDGMENTS

W. M. acknowledges financial support from the Polish National Agency for Academic Exchange under decision BPN/BEK/2022/1/00179/DEC/1. J. R. and J. Á. C.-R. acknowledge support from the Swedish Research Council, the Olle Engkvist Foundation, and the Knut and Alice

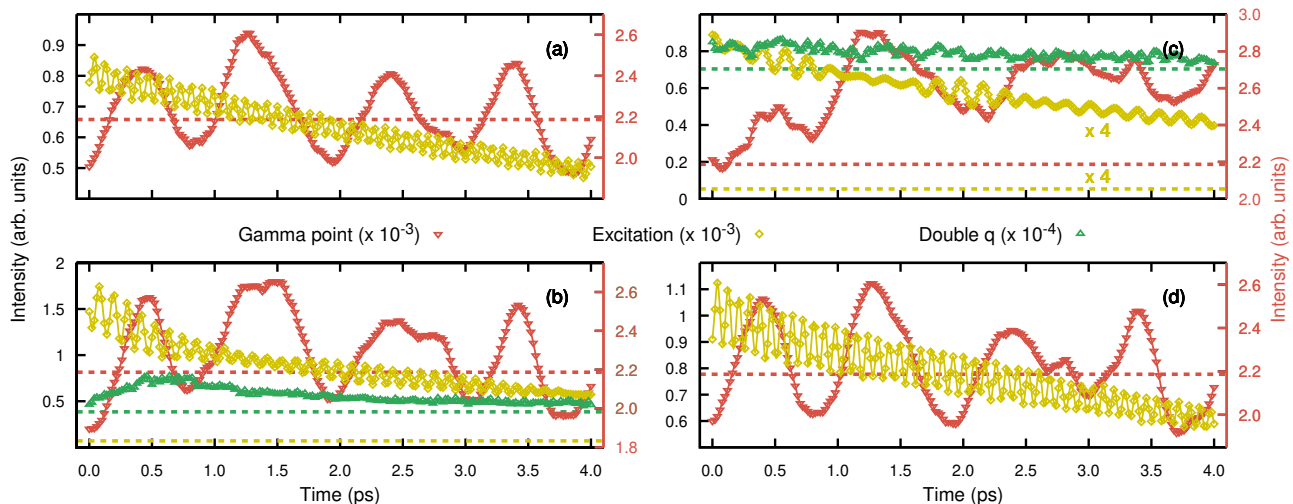


FIG. 7: Integrated diffraction intensities over a longer, 4 ps, trajectory with a sampling period of 20 fs. Panel (a) shows the relaxation of the excitation at the X-point in the \hat{q}_y direction. Panel (b) depicts the relaxation along the Δ high-symmetry line in the \hat{q}_y direction, halfway between the Γ and X points. Panel (c) presents relaxation along the Δ high-symmetry line in the \hat{q}_y direction at half the frequency of the X-point. Panel (d) shows the relaxation of the excitation at the X-point in the \hat{q}_z direction. The plots correspond to the relaxation processes of the excitations shown in Fig. 5, with matching colors and panel order. For panels (a) and (d), the equilibrium values at 325 K for the intensity integrated over the excitation point (yellow curve) reach values 3.85×10^{-5} and 5.06×10^{-5} , which are outside the plotted region.

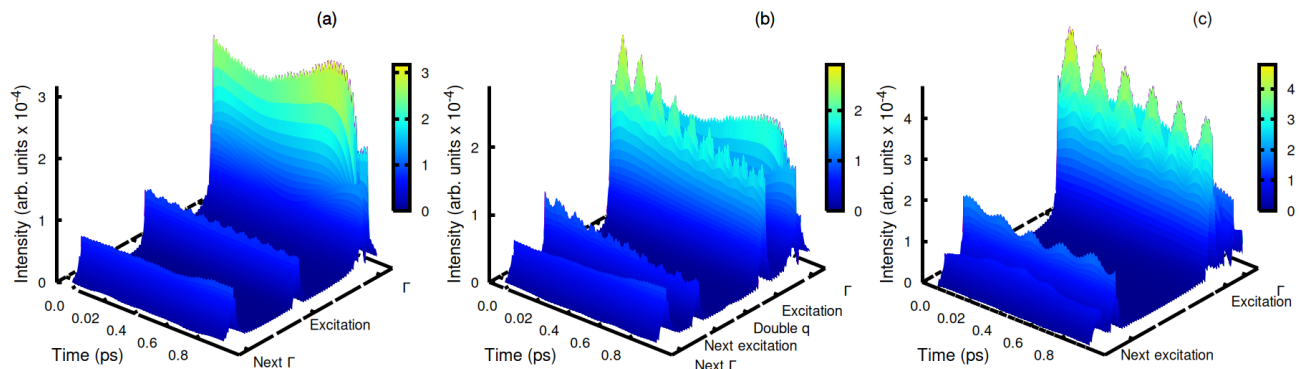


FIG. 8: Diffraction intensities along the Δ ($\Gamma - X$) high symmetry line: a) Excitation in X point in \hat{q}_y direction; b) Excitation along the Δ high symmetry line in \hat{q}_y direction and in half the way between Γ and X high symmetry points; c) Excitation along the Δ high symmetry line in \hat{q}_y direction and in half frequency of X point. Plots present the relaxation process of excitations presented in Fig. 5, present a broader range of data presented in more detail in Fig. 7, and use the respective order of panels.

Wallenberg Foundation. The simulations were enabled by resources provided by the National Academic Infras-

tructure for Supercomputing in Sweden (NAISS) at NSC Centre, partially funded by the Swedish Research Council through grant agreement no. 2022-06725.

[1] E. Beaurepaire, J.-C. Merle, A. Daunois, and J.-Y. Bigot, Ultrafast spin dynamics in ferromagnetic nickel, *Phys. Rev. Lett.* **76**, 4250 (1996).

[2] B. Koopmans, G. Malinowski, F. Dalla Longa, D. Steiauf, M. Fähnle, T. Roth, M. Cinchetti, and M. Aeschliemann, Explaining the paradoxical diversity of ultrafast

- laser-induced demagnetization, *Nature Materials* **9**, 259 (2010).
- [3] D. Zahn, F. Jakobs, Y. W. Windsor, H. Seiler, T. Vasileiadis, T. A. Butcher, Y. Qi, D. Engel, U. Atxitia, J. Vorberger, and R. Ernstorfer, Lattice dynamics and ultrafast energy flow between electrons, spins, and phonons in a 3d ferromagnet, *Phys. Rev. Res.* **3**, 023032 (2021).
- [4] M. Pankratova, I. P. Miranda, D. Thonig, M. Pereiro, E. Sjöqvist, A. Delin, O. Eriksson, and A. Bergman, Heat-conserving three-temperature model for ultrafast demagnetization in nickel, *Phys. Rev. B* **106**, 174407 (2022).
- [5] M. Battiato, K. Carva, and P. M. Oppeneer, Superdiffusive spin transport as a mechanism of ultrafast demagnetization, *Phys. Rev. Lett.* **105**, 027203 (2010).
- [6] T. Roth, A. J. Schellekens, S. Alebrand, O. Schmitt, D. Steil, B. Koopmans, M. Cinchetti, and M. Aeschliemann, Temperature dependence of laser-induced demagnetization in ni: A key for identifying the underlying mechanism, *Phys. Rev. X* **2**, 021006 (2012).
- [7] C. Dornes, Y. Acremann, M. Savoini, M. Kubli, M. J. Neugebauer, E. Abreu, L. Huber, G. Lantz, C. A. F. Vaz, H. Lemke, E. M. Bothschafter, M. Porer, V. Esposito, L. Rettig, M. Buzzi, A. Alberca, Y. W. Windsor, P. Beaud, U. Staub, D. Zhu, S. Song, J. M. Glownia, and S. L. Johnson, The ultrafast einstein–de haas effect, *Nature* **565**, 209 (2019).
- [8] P. Maldonado, T. Chase, A. H. Reid, X. Shen, R. K. Li, K. Carva, T. Payer, M. Horn von Hoegen, K. Sokolowski-Tinten, X. J. Wang, P. M. Oppeneer, and H. A. Dürr, Tracking the ultrafast nonequilibrium energy flow between electronic and lattice degrees of freedom in crystalline nickel, *Phys. Rev. B* **101**, 100302 (2020).
- [9] U. Ritzmann, P. M. Oppeneer, and P. Maldonado, Theory of out-of-equilibrium electron and phonon dynamics in metals after femtosecond laser excitation, *Phys. Rev. B* **102**, 214305 (2020).
- [10] S. R. Tauchert, M. Volkov, D. Ehberger, D. Kazenwadel, M. Evers, H. Lange, A. Donges, A. Book, W. Kreuzpaintner, U. Nowak, and P. Baum, Polarized phonons carry angular momentum in ultrafast demagnetization, *Nature* **602**, 73 (2022).
- [11] M. Haider, S. Uhlemann, E. Schwan, H. Rose, B. Kabius, and K. Urban, Electron microscopy image enhanced, *Nature* **392**, 768 (1998).
- [12] P. E. Batson, N. Dellby, and O. L. Krivanek, Sub-ångstrom resolution using aberration corrected electron optics, *Nature* **418**, 617 (2002).
- [13] O. L. Krivanek, T. C. Lovejoy, N. Dellby, T. Aoki, R. W. Carpenter, P. Rez, E. Soignard, J. Zhu, P. E. Batson, M. J. Lagos, R. F. Egerton, and P. A. Crozier, Vibrational spectroscopy in the electron microscope, *Nature* **514**, 209 (2014).
- [14] X. Li, P. Mooney, S. Zheng, C. R. Booth, M. B. Braunschweig, S. Gubbens, D. A. Agard, and Y. Cheng, Electron counting and beam-induced motion correction enable near-atomic-resolution single-particle cryo-em, *Nature Methods* **10**, 584 (2013).
- [15] J. L. Hart, A. C. Lang, A. C. Leff, P. Longo, C. Trevor, R. D. Twisten, and M. L. Taheri, Direct detection electron energy-loss spectroscopy: A method to push the limits of resolution and sensitivity, *Scientific Reports* **7**, 8243 (2017).
- [16] A. H. Zewail, Four-dimensional electron microscopy, *Science* **328**, 187 (2010), <https://www.science.org/doi/pdf/10.1126/science.1166135>.
- [17] A. Feist, N. Bach, N. Rubiano da Silva, T. Danz, M. Möller, K. E. Priebe, T. Domröse, J. G. Gatzmann, S. Rost, J. Schauss, S. Strauch, R. Bormann, M. Sivis, S. Schäfer, and C. Ropers, Ultrafast transmission electron microscopy using a laser-driven field emitter: Femtosecond resolution with a high coherence electron beam, *Ultramicroscopy* **176**, 63 (2017), 70th Birthday of Robert Sinclair and 65th Birthday of Nestor J. Zaluzec PICO 2017 – Fourth Conference on Frontiers of Aberration Corrected Electron Microscopy.
- [18] J. H. Gaida, H. Lourenço-Martins, M. Sivis, T. Rittmann, A. Feist, F. J. García de Abajo, and C. Ropers, Attosecond electron microscopy by free-electron homodyne detection, *Nature Photonics* **18**, 509 (2024).
- [19] H.-W. N. Ye-Jin Kim, Won-Woo Park and O.-H. Kwon, High-resolution correlative imaging in ultrafast electron microscopy, *Advances in Physics: X* **9**, 2316710 (2024), <https://doi.org/10.1080/23746149.2024.2316710>.
- [20] A. P. Thompson, H. M. Aktulga, R. Berger, D. S. Bolintineanu, W. M. Brown, P. S. Crozier, P. J. in 't Veld, A. Kohlmeyer, S. G. Moore, T. D. Nguyen, R. Shan, M. J. Stevens, J. Tranchida, C. Trott, and S. J. Plimpton, LAMMPS - a flexible simulation tool for particle-based materials modeling at the atomic, meso, and continuum scales, *Comput. Phys. Commun.* **271**, 108171 (2022).
- [21] R. F. Loane, P. Xu, and J. Silcox, Thermal vibrations in convergent-beam electron diffraction, *Acta Cryst A* **47**, 267 (1991).
- [22] J. Barthel, Dr. Probe: A software for high-resolution STEM image simulation, *Ultramicroscopy* **193**, 1 (2018).
- [23] P. M. Zeiger and J. Ruzs, Efficient and Versatile Model for Vibrational STEM-EELS, *Phys. Rev. Lett.* **124**, 025501 (2020).
- [24] P. M. Zeiger and J. Ruzs, Frequency-resolved frozen phonon multislice method and its application to vibrational electron energy loss spectroscopy using parallel illumination, *Phys. Rev. B* **104**, 104301 (2021).
- [25] M. Frigo and S. Johnson, The Design and Implementation of FFTW3, *Proc. IEEE* **93**, 216 (2005).
- [26] A. P. Thompson, L. P. Swiler, C. R. Trott, S. M. Foiles, and G. J. Tucker, Spectral neighbor analysis method for automated generation of quantum-accurate interatomic potentials, *J. Comput. Phys.* **285**, 316 (2015).
- [27] Y. Zuo, C. Chen, X. Li, Z. Deng, Y. Chen, J. Behler, G. Csányi, A. V. Shapeev, A. P. Thompson, M. A. Wood, and S. P. Ong, Performance and Cost Assessment of Machine Learning Interatomic Potentials, *J. Phys. Chem. A* **124**, 731 (2020).
- [28] M. E. Tuckerman, J. Alejandre, R. López-Rendón, A. L. Jochim, and G. J. Martyna, A Liouville-operator derived measure-preserving integrator for molecular dynamics simulations in the isothermal-isobaric ensemble, *J. Phys. A: Math. Gen.* **39**, 5629 (2006).
- [29] M. Parrinello and A. Rahman, Polymorphic transitions in single crystals: A new molecular dynamics method, *J. Appl. Phys.* **52**, 7182 (1981).
- [30] W. Shinoda, M. Shiga, and M. Mikami, Rapid estimation of elastic constants by molecular dynamics simulation under constant stress, *Phys. Rev. B* **69**, 134103 (2004).
- [31] J. Tukey, An introduction to the calculation of numerical spectrum analysis, *Spectra Analysis of Time Series*, 25 (1967).

- [32] R. J. Birgeneau, J. Cordes, G. Dolling, and A. D. B. Woods, Normal Modes of Vibration in Nickel, *Phys. Rev.* **136**, A1359 (1964).
- [33] C. Lee, D. Vanderbilt, K. Laasonen, R. Car, and M. Parrinello, Ab initio studies on the structural and dynamical properties of ice, *Phys. Rev. B* **47**, 4863 (1993).
- [34] A. Carreras, A. Togo, and I. Tanaka, DynaPhoPy: A code for extracting phonon quasiparticles from molecular dynamics simulations, *Computer Physics Communications* **221**, 221 (2017).
- [35] Note, that the authors in Ref. [34] worked with velocities, which are phase-shifted in relation to the displacements.
- [36] B. D. Forbes, A. V. Martin, S. D. Findlay, A. J. D'Alfonso, and L. J. Allen, Quantum mechanical model for phonon excitation in electron diffraction and imaging using a born-oppenheimer approximation, *Phys. Rev. B* **82**, 104103 (2010).
- [37] N. R. Lugg, B. D. Forbes, S. D. Findlay, and L. J. Allen, Atomic resolution imaging using electron energy-loss phonon spectroscopy, *Phys. Rev. B* **91**, 144108 (2015).
- [38] F. Qi, Z. Ma, L. Zhao, Y. Cheng, W. Jiang, C. Lu, T. Jiang, D. Qian, Z. Wang, W. Zhang, P. Zhu, X. Zou, W. Wan, D. Xiang, and J. Zhang, Breaking 50 Femtosecond Resolution Barrier in MeV Ultrafast Electron Diffraction with a Double Bend Achromat Compressor, *Phys. Rev. Lett.* **124**, 134803 (2020).
- [39] K. Sokolowski-Tinten, C. Blome, J. Blums, A. Cavalleri, C. Dietrich, A. Tarasevitch, I. Uschmann, E. Förster, M. Kammler, M. Horn-von-Hoegen, and D. von der Linde, Femtosecond X-ray measurement of coherent lattice vibrations near the Lindemann stability limit, *Nature* **422**, 287 (2003).
- [40] M. Harmand, R. Coffee, M. R. Bionta, M. Chollet, D. French, D. Zhu, D. M. Fritz, H. T. Lemke, N. Medvedev, B. Ziaja, S. Toleikis, and M. Cammarata, Achieving few-femtosecond time-sorting at hard X-ray free-electron lasers, *Nature Photon* **7**, 215 (2013).
- [41] D. M. Fritz, D. A. Reis, B. Adams, R. A. Akre, J. Arthur, C. Blome, P. H. Bucksbaum, A. L. Cavalieri, S. Enghemann, S. Fahy, R. W. Falcone, P. H. Fuoss, K. J. Gaffney, M. J. George, J. Hajdu, M. P. Hertlein, P. B. Hillyard, M. Horn-von Hoegen, M. Kammler, J. Kaspar, R. Kienberger, P. Krejcik, S. H. Lee, A. M. Lindenberg, B. McFarland, D. Meyer, T. Montagne, E. D. Murray, A. J. Nelson, M. Nicoul, R. Pahl, J. Rudati, H. Schlarb, D. P. Siddons, K. Sokolowski-Tinten, Th. Tschentscher, D. von der Linde, and J. B. Hastings, Ultrafast Bond Softening in Bismuth: Mapping a Solid's Interatomic Potential with X-rays, *Science* **315**, 633 (2007).
- [42] L. Zhao, J. Wu, Z. Wang, H. Tang, X. Zou, T. Jiang, P. Zhu, D. Xiang, and J. Zhang, Noninvasive time-sorting in radio frequency-compressed ultrafast electron diffraction, *Structural Dynamics* **8**, 044303 (2021).